ACS Catalysis

pubs.acs.org/acscatalysis

Research Article

Efforts Toward Unraveling Plasma-Assisted Catalysis: Determination of Kinetics and Molecular Temperatures within N_2O Discharges

Angela R. Hanna and Ellen R. Fisher*

Cite This: *ACS Catal.* 2020, 10, 6546−6560

Read Online

ACCESS | Metrics & More | Article Recommendations | Supporting Information

ABSTRACT: Plasma-assisted catalysis represents an alternative solution to pollution abatement. To be viable, a thorough understanding of plasma−catalyst synergisms must be gained, specifically establishing links between the gas-phase, gas−surface interface, and resulting material properties. Optical emission spectroscopy provides insights into the impact of Pt and zeolite catalysts on plasma species densities, energetics, reaction kinetics, and plasma−catalyst configurations within N_2O plasmas. The role of material structure on gas-phase chemistry is revealed through the use of Pt catalysts with two morphologies and size scaling. The concentration of excited-state NO substantially decreased at high powers with Pt nanopowder or microstructured zeolites. All catalytic materials significantly decreased N_2 vibrational temperatures, with little impact on rotational temperatures. Conversely, Pt materials had a limited effect on vibrational temperatures of NO; however, Pt powder enhanced NO decomposition within a two-stage system over the single-stage system. Material characterization revealed that the plasma effectively poisons Pt materials, resulting in poorer performance.

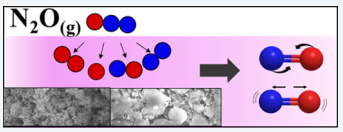

KEYWORDS: *plasma-assisted catalysis, nitrogen oxides, zeolites, energy partitioning, plasma kinetics*

1. INTRODUCTION

N_2O is a greenhouse gas that contributes to ozone depletion,[1] has a greenhouse warming potential ∼300 times that of CO_2, and can remain in the atmosphere for an average of 114 years.[2] N_2O is produced through natural processes; however, it is largely emitted from anthropogenic sources, including wastewater management, industrial processes, agriculture, and fuel combustion. The continuous increase of N_2O in the atmosphere, combined with long atmospheric residence times, requires developing efficient solutions for its abatement. Thermal decomposition,[3] selective adsorption,[4,5] catalytic decomposition, and plasma technologies[6,7] have been studied as means to reduce and remove N_2O emissions in the atmosphere. Catalytic decomposition offers several advantages for reducing N_2O emissions, including decreased energy requirements and an enhanced rate of conversion. Prior investigations have shown that N_2O decomposes via a first-order reaction, where proposed general reaction schemes for its catalytic decomposition are shown in reactions 1 and 2.[8,9]

$$\text{catalyst} + N_2O_{(g)} \rightarrow N_{2(g)} + O_{(ads)} \quad (1)$$

$$O_{(ads)} + N_2O_{(g)} \rightarrow N_{2(g)} + O_{2\ (ads)} \quad (2)$$

Several catalysts have been examined for N_2O decomposition, including noble metals (Pt, Au, and Pd),[10] metal oxides (TiO_2, NiO, Fe_2O_3, and ZnO),[8,11] mixed metal oxides,[12,13] zeolites (ZSM-5, ZSM-11, and Ferrierite),[4,14,15] and perovskite-type oxides.[16] Although these catalysts show high removal efficiency, they can also require operating temperatures >300 °C. To improve energy efficiency and selectivity of these processes, plasma-assisted catalysis (PAC) has been explored as a promising alternative technology for pollution abatement.[17−19]

Although auspicious, the applicability of PAC is limited due to a paucity of knowledge of the nature of fundamental plasma−catalyst interactions. Currently, there are three PAC techniques actively investigated, including two different configurations of two-stage systems, wherein the catalyst and plasma are physically separated, as well as single-stage systems wherein the catalyst is placed directly in the discharge.[20,21] Within two-stage systems, the plasma alters the gas-phase composition, either prior to or after interaction with the catalyst, whereas single-stage systems enable all plasma species to interact with the catalyst simultaneously, often resulting in diverse dissociation products and significant alteration to the surface properties of the catalyst. Thus, deciphering possible synergisms within single-stage PAC systems is complex, originating from the discharge-catalyst interdependence.

The principles of PAC can be applied across a wide range of waste treatments, not limited to the oxidation of volatile organic compounds,[22] ammonia synthesis,[23] and methanation of CO_2;[24] however, NO_x emissions are of particular interest. Hur et al. studied the decomposition of N_2O in a low-pressure reactor, finding the destruction and removal efficiency (DRE) of N_2O enhanced by increasing applied power from 1.3 to

Received: February 16, 2020
Revised: May 9, 2020
Published: May 27, 2020

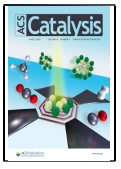

https://dx.doi.org/10.1021/acscatal.0c00794
ACS Catal. 2020, 10, 6546−6560

1.8 kW.[25] Jo et al. investigated the decomposition of N_2O over gamma alumina-supported metal oxide catalysts, revealing that decomposition efficiency tends to decrease with increasing amounts of O_2 in the feed gas.[12] This result suggests that gas-phase species compete for active sites on the catalyst and the adsorption of oxygen onto these active sites could inhibit the decomposition of N_2O.[12] This hypothesis was further supported by the work completed by Fan et al., documenting a substantial decrease in N_2O conversion with the concomitant increase of O_2 content in a N_2-O_2 mixture.[26] The type of plasma discharge (e.g., gliding arc, dielectric barrier, radio frequency, etc.), chemical nature, and material morphology are all capable of modifying plasma−catalytic processes. Affordable materials (compared to rare-earth metals) with complex morphologies (specifically nano- and microstructured materials) could have an advantageous impact on PAC processes. Increasing the surface area to volume ratio for a catalyst could initiate additional surface interactions between the plasma species and material, synergistically combining to result in augmented decomposition of a waste stream. Numerous studies have, therefore, focused on ion-exchanged Zeolite Socony Mobil (ZSM)-5 zeolites. Specifically, Centi et al.[4] and Guillemot and Castel[27] found Ba-ZSM-5 to be a successful material in N_2O treatment applications. The addition of an active material can clearly impact the plasma itself; therefore, it is crucial to characterize gas-phase species with and without a catalyst in the system.

We have previously studied emitting and absorbing species in N_2O discharges,[28] determining that rotational (T_R) and vibrational (T_V) temperatures for both N_2 and NO molecules increase with increasing applied rf power (P) and decrease with increasing system pressure (p). This suggests that as more energy is supplied to the discharge through increasing applied power, this energy is transferred to the gas-phase molecules, thereby populating higher vibrational states. As system pressure increases, the number of collisions within the plasma concomitantly increases, resulting in decreased T_R and T_V values through collisional quenching. Initial time-resolved optical emission spectroscopy (TR-OES) experiments suggested a mechanism of direct, electron impact excitation of NO from both NO and N_2O precursors.[28] Through the combination of energetic and kinetic information, we can begin to optimize plasma operating conditions for the increased decomposition of N_2O into ambient species (e.g., N_2 and O_2) and decrease the amount of NO formed in a discharge.

In this work, these foundational plasma studies were expanded to investigate the decomposition of N_2O over Pt and zeolite catalysts. By selecting two forms of the same catalyst, Pt in foil and the nanopowder form, the influence of material morphology on the discharge can be deduced, nominally without the complication of large differences in chemical identity. In addition to the rare-earth metal catalysts, microstructured aluminosilicate zeolites were studied herein. Of burgeoning interest is the correlation between material properties (e.g., chemical identity and pore size) and their potential influence on plasma properties (e.g., species density, energy distributions, and formation of microplasmas within pores). Significant research efforts have been focused toward understanding the scaling of microplasmas in porous materials;[17,29] therefore, we also sought to characterize the impact of both nano- and microscale materials on plasma thermodynamics and kinetics. By focusing on these plasma properties, the experiments and results herein will produce foundational data for addressing critical intellectual challenges in the field of plasma science.[17] Collectively, this approach can advance globally relevant technologies by providing pathways to better processes and materials for pollution abatement via PAC.

2. METHODS

2.1. General. Inductively coupled plasmas were formed in a glass tubular reactor (Figure 1a) described in detail previously.[30] Briefly, precursor gases entered the reactor where pressure was maintained via a rotary vane mechanical pump, monitored with a Baratron capacitance manometer. The base pressure of this apparatus was ∼1 mTorr; system pressure was 100 mTorr above base for all studies herein (total system pressure of ∼101 mTorr). A 13.56 MHz radio frequency (rf) power supply was coupled to an eight-turn nickel-plated copper coil to ignite the plasma discharge, with P ranging from 25 to 175 W. For single-stage catalysis studies (Figure 1a), materials were placed in the center of the coil to examine the effects of catalytic materials on gas-phase chemistry. For two-stage studies, a pre-plasma catalysis system was constructed (Figure 1b) that included a stainless steel vacuum chamber mated upstream to the plasma reactor. Catalysts were placed in the center of this chamber; feed gas flowed over the material and entered the glass reactor, and a plasma was subsequently ignited.

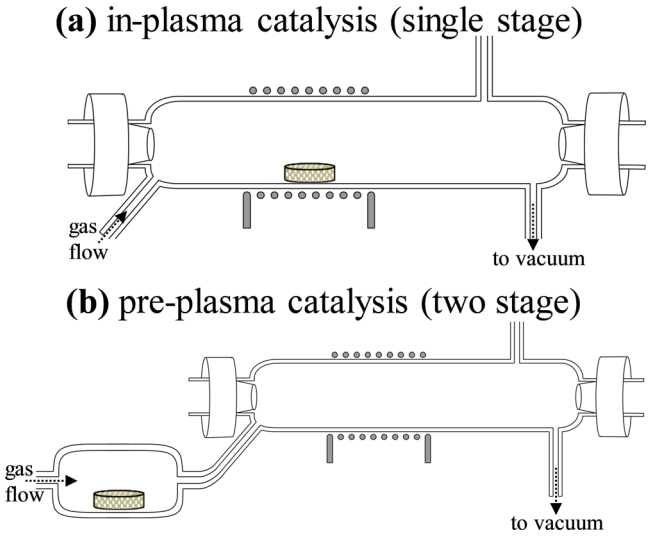

Figure 1. Schematic representation of (a) single-stage PAC reactor, wherein materials are placed directly in the coil region, and (b) two-stage, pre-plasma catalysis PAC setup, wherein gas flows over the catalyst then enters the plasma reactor.

Platinum foil (Alfa Aesar, 99.99%, 0.025 mm), platinum powder (Alfa Aesar, 99.99%, 9−19 m^2/g), and Na^+ zeolite (Sigma Aldrich, 13×, 45/60 mesh molecular sieves) catalysts were studied. For each material, samples were prepared in the same manner with the same specifications to mitigate sample variability. Commercial Pt foil was employed as received and cut into 4 cm × 1 cm rectangles, and Pt powder was secured to glass slides (VWR) with double-sided carbon tape (VWR). Pt powder substrates were 4 cm × 0.5 cm, with ∼0.15 g of nanopowder mounted on the glass slide. Molecular sieves were ground with a mortar and pestle into a fine powder with an

https://dx.doi.org/10.1021/acscatal.0c00794
ACS Catal. 2020, 10, 6546−6560

experimentally determined specific surface area of 930 m^2 g^{-1} then placed in an 18,000 psi pellet press (Carver) to create 0.3 g of zeolite pellets (13 mm × 2 mm).[31] In specific studies, Pt nanopowder and zeolite pellets were oven-calcinated at 150 °C for 3 h. The precursor gases used were N_2O (Airgas, >99%) and Ar (Airgas, >99.999%). Reported gas ratios are based on the partial pressure of each constituent of the feed gas; small amounts of Ar were added to the feed as an inert gas actinometer in specified gas-phase studies.

2.2. Gas-Phase Plasma Diagnostics. Plasma emission was collected by an AvaSpec-2048L-USB2-RM multichannel spectrometer via a fiber optic cable and collimating lens described previously.[28,30] The spectrometer houses six fiber optic gratings mated to six 2048 pixel charge-coupled device array detectors, resulting in a wavelength collection range of 200−1000 nm with an ∼0.1 nm spectral resolution. Inert gas actinometry was used to elucidate steady-state relative species densities, utilizing the 750.4 nm emission line of Ar. Steady-state experiments were collected at 150 ms, with 50 averages over a minimum of ten scans. Time-resolved actinometry studies were collected at 50 ms, with 5 averages (0.25 s/data point) for 60 s. Described previously,[32] time-resolved OES (TR-OES) was also used to quantify rate constants without the presence of Ar. Data collection began before plasma ignition and lasted for ∼4 s after ignition with a 1.5 ms integration time. TR-OES was collected with an AvaSpec-ULS4096CL-EVO spectrometer configured with a 10 μm slit. The intensity of signals arising from excited-state NO (235.9 nm) and N_2 (337.0 nm) was monitored as a function of time. The rise to maximum intensity was identified and fit with a first-order exponential function to compute a rate constant of formation (k_f), and the subsequent decrease in signal intensity to a steady-state is denoted here as the rate constant of destruction (k_d), which is not present in all cases. The temporal evolution of N_2 and NO emissions is depicted in Figure S1a,b, respectively. N_2 and NO rate constants, as well as the relative goodness of each exponential fit, are reported.

Energy partitioning trends as a function of applied rf power and catalyst were elucidated by investigating the NO gamma ($X^2\Pi-A^2\Sigma^+$) and N_2 second positive ($B^3\Pi_g-C^2\Pi_u$) transitions, shown in Figure S2a. Briefly, T_R and T_V for excited-state NO molecules were computed using LIFBASE[33] by adjusting the T_R values to best match the experimental peak full width half maximum (FWHM), assuming a thermalized rotational distribution, to yield a rotational temperature. T_V (NO) values were determined by the summation of vibrational energy for each populated vibrational level over the wavelength range of 200−280 nm within LIFBASE, weighted by Boltzmann's constant (k_B). T_R (N_2) values were calculated using the Specair program.[34] T_R (N_2 and NO) and T_V (NO) within an N_2O (gas only) system were previously reported and are included herein to probe the difference in plasma energetics upon addition of a material.[28] T_V (N_2) values were also reported previously;[28] however, those values were determined using the "Temperature Loop" function within Specair.[34] Here, the Boltzmann plot method was used to compute T_V (N_2) using vibrational transitions of the second positive system ($B^3\Pi_g-C^2\Pi_u$) in the wavelength range of 262−376 nm, assuming a Boltzmann distribution. This wide wavelength range was selected to adequately represent the entirety of the N_2 emission band. The line intensity, I (a.u.), corresponding to the transition at a given wavelength (λ) from an upper vibrational level, ν', to a lower vibrational level, ν'', is given by the following formula

$$I_{\nu'-\nu''} \propto hc\nu A_{\nu'-\nu''}\exp\left(\frac{E}{k_B T_V}\right) \quad (3)$$

where h is the Planck constant, c is the velocity of light, A (s^{-1}) is the corresponding Franck−Condon factor for the vibrational transition. The slope of the Boltzmann plot is proportional to $1/T_V$. A representative Boltzmann plot is depicted in Figure S2b for N_2 in a N_2O plasma with a zeolite pellet, generated from the emission spectrum and the spectroscopic information provided previously.[31] To probe the impact of catalysts on the vibrational temperatures, ΔT_V was calculated via eq 4, where the error reported was appropriately propagated.

$$\Delta T_V = [T_V(\text{catalyst}) - T_V(\text{no substrate})] \quad (4)$$

2.3. Material Characterization. X-ray photoelectron spectroscopy (XPS) was performed on a Physical Electronics PE5800 ESCA/AES system with a monochromatic Al Kα X-ray source (1486.6 eV), hemispherical analyzer, and multichannel detector to provide information on surface composition and binding environments. Survey spectra were collected for 2 min from 10 to 1100 eV (pass energy = 187.9 eV, resolution = 0.80 eV). High-resolution spectra (pass energy = 23.5 eV, resolution = 0.10 eV) were collected for 20 min for all elements with compositions >2% from survey spectra. High-resolution spectra were used for all quantification, specifically measuring atomic composition of catalysts before and after plasma exposure. Charge correction and fitting of high-resolution spectra were performed with CasaXPS, spectra were charge-corrected setting the −C−C/C−H peak in the C 1s spectrum to 284.8 eV, and the FWHM value for each binding environment was constrained to be ≤2.0 eV. A minimum of three spots on three samples (n = 9) was collected, where a mean value and its standard deviation are reported. Scanning electron microscopy (SEM) was performed using a JEOL JSM-6500F microscope to qualitatively evaluate material architecture, operating with an accelerating voltage of 15 kV and a working distance of 10 mm. Energy-dispersive spectroscopy (EDS) was performed in conjunction with SEM to obtain elemental composition maps of Pt materials. Powder X-ray diffraction (PXRD) data were obtained via a Bruker D8 Discover DaVinci powder X-ray diffractometer with a Cu Kα radiation source using 2θ from 5 to 80° at intervals of 0.02° with scans of 0.5 step/s to access the bulk crystallinity of catalytic materials before and after plasma treatment.

3. RESULTS

A major focus of this work is to explore the potential of Pt and zeolites as catalysts in the plasma-assisted decomposition of N_2O. One key element of these studies examines the impact of material morphology on the overall process. Pt foil (Figure 2a) shows a relatively smooth morphology; however, scratches and imperfections can be seen at higher (65×) magnification. The Pt powder (Figure 2b) displays a random, highly porous network with minimum agglomeration of nanoparticle clusters. Microstructured zeolite pellets (Figure 2c) also display an interconnected porous morphology.

Using inert-gas actinometry, the relative densities of excited-state plasma species (denoted here with brackets, e.g., "[NO]") observed in N_2O systems, with and without catalysts, can be evaluated. Depicted in Figure 3, relative densities of N_2

https://dx.doi.org/10.1021/acscatal.0c00794
ACS Catal. 2020, 10, 6546−6560

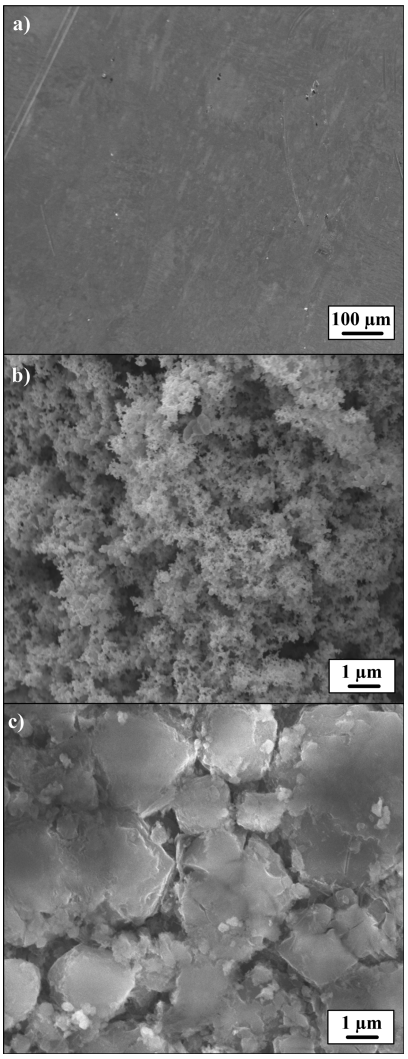

Figure 2. SEM images of (a) Pt foil (65×), (b) Pt powder (5000×), and (c) zeolite pellet (5000×).

(337.0 nm, Figure 3a), NO (235.9 nm, Figure 3b), atomic O (777.2 nm, Figure 3c), and OH (309.0 nm, Figure 3d) generated from a 90:10 N_2O/Ar plasma are plotted as a function of power for the gas only system and with Pt foil, Pt powder, or zeolites in the coil region of the reactor (Figure 1a). With no material in the plasma discharge, [N_2] slightly decreases with a concomitant increase of [NO], [O], and [OH] as P increases from 25 to 175 W, suggesting additional fragmentation of N_2O at higher power. At 25−75 W, the relative densities of N_2 and NO are higher with Pt foil present compared to the material-free system, ultimately converging to values within the experimental error of each other as P increases to 175 W. The Pt foil system also demonstrates an increase in [O] with power, yet more atomic oxygen is present in the material-free system at all P except 175 W. The nanostructured Pt powder (Figure 3b) resulted in a decrease in excited-state N_2 and NO with a corresponding increase in atomic O. These data clearly highlight the impact of material morphology; although both are nominally platinum, there is a significant and measurable difference in the resulting gas-phase chemistry. The influence of material morphology on the resulting decomposition of N_2O is discussed below. Furthermore, the amount of OH in the discharge is substantially increased at higher P with Pt powder present, a trend that continues with the microporous zeolite pellet. To further investigate the production of OH in the discharge, zeolite pellets were oven-calcinated to remove adsorbed H_2O, and inert-gas actinometry was performed at P = 175 W with the oven-calcinated pellets, shown in Figure S3. The amount of OH in the discharge with an oven-calcinated zeolite pellet only slightly decreased, suggesting $OH_{(g)}$ is formed from plasma−catalyst interactions, further discussed below.

Unlike the other catalytic materials, a sharp increase in [N_2] and corresponding decrease in [NO] are measured at $P \geq$ 75 W with a zeolite pellet in the coil. Notably, all data provided in Figure 3 were collected over several minutes, averaging multiple spectra collected with a 50 ms integration time, 150 averages per scan. As such, these effectively steady-state measurements can clearly provide insights into plasma−catalyst interactions. Nevertheless, optical spectroscopy can also be employed to gain temporally resolved information about these plasma−catalyst systems.

The presence of a zeolite pellet in a N_2O plasma resulted in the smallest amount of NO produced in the discharge. As such, actinometric TR-OES data were collected with a zeolite pellet in the system at two P (Figure 4). Relative intensities of N_2 (orange), NO (blue), O (green), and OH (gray) were monitored via TR-OES as a function of time. At P = 25 W, [N_2] increases as a function of time, reaching an intensity maximum after ∼12 s. A subsequent decay to an apparent steady-state density occurred as time increases to 60 s. When P is increased to 150 W, [N_2] gradually increases over the 60 s collection time, in contrast to the lower P data. Figure 4b is plotted with a logarithmic y-axis to more easily distinguish species at low concentrations. Note also that there is a gradual decrease in [NO] over time in the 25 W system, whereas in the 150 W system, [NO] signals became erratic and are only slightly above experimental noise after ∼35 s. [O] increased throughout the plasma duration at 150 W compared to the 25 W discharge, where an initial increase and slight decay to a steady state were measured. In contrast, the [OH] in the discharge at 25 W did not change over time, further supporting the observation that there is little to no OH in the system with these conditions (Figure 3d). At higher P, the [OH] increases significantly with time, exceeding the [O] after ∼35 s. Particularly noticeable in the 150 W system, the first few points (<5 s) are scattered for all species; thus, selected species were studied with a higher time resolution to elucidate how they are initially formed and interact within the discharge.

TR-OES was performed without the addition of Ar to study the first 4 s of plasma ignition, employing a 1.5 ms integration time. As described above, using a first-order exponential function to fit the onset of OES signals for N_2 and NO, k_f (s^{-1}) values were determined and are depicted as a function of P in Figure 5a,b, respectively. N_2 and NO k_f values are also reported in Table 1; k_d (NO) values are included in Table 2. k_f (N_2) values increased with increasing power for the gas only, Pt powder, and zeolite systems, ranging from 1.484 s^{-1} (zeolite, 25 W) to 17.579 s^{-1} (Pt powder, 150 W). Note, 150 W is the highest applied power examined in the time-resolved studies compared to 175 W in the steady-state experiments. At P = 175 W, plasma ignition was influenced by reflected rf P fluctuations within the first μs; therefore, rate constants could not be reliably quantified. Moreover, [NO] (and therefore NO signal) in the discharge is low at P = 175 W for both Pt powder and zeolite systems. At all P, excluding 125 W, k_f (N_2) with Pt

https://dx.doi.org/10.1021/acscatal.0c00794
ACS Catal. 2020, 10, 6546−6560

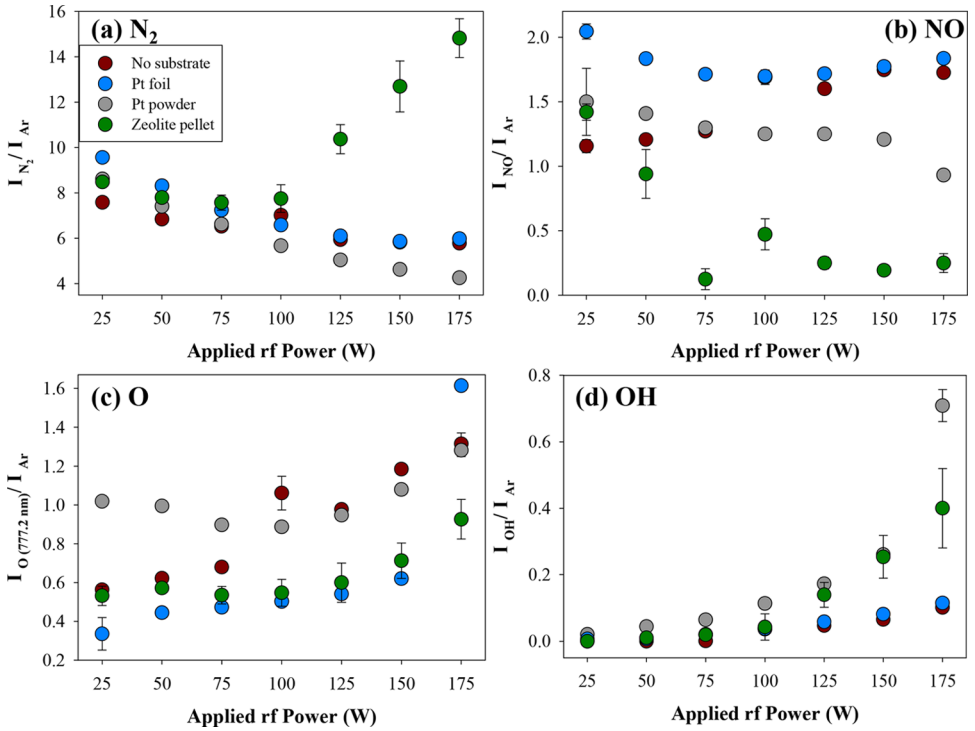

Figure 3. Relative density of (a) N_2, (b) NO, (c) O, and (d) OH as a function of P in a 100 mTorr, single-stage N_2O plasma system. Error bars are plotted for all points and represent one standard deviation from the mean ($n \geq 3$).

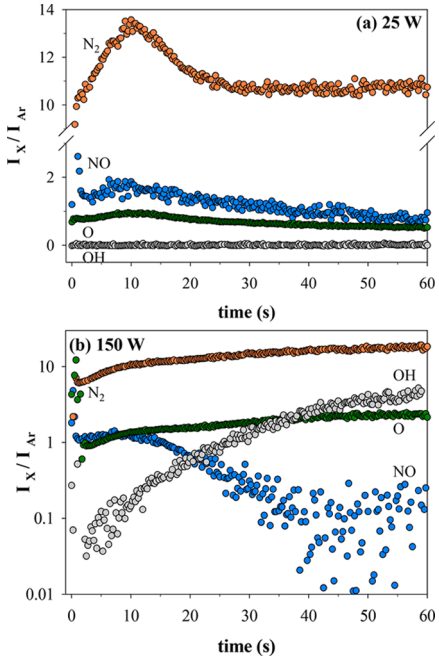

Figure 4. Relative intensity of plasma species (X) as a function of time for a 100 mTorr 90/10 N_2O/Ar plasma at (a) 25 W and (b) 150 W, with a zeolite pellet present in the coil region of the discharge. Note that relative intensities are plotted on (a) linear and (b) log scales.

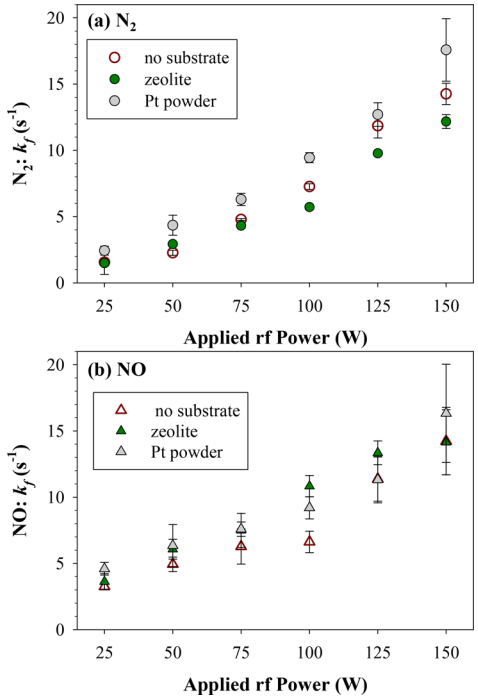

Figure 5. k_f (s^{-1}) for (a) N_2 and (b) NO plotted as a function of P and material. Error bars represent one standard deviation from the mean ($n \geq 6$).

powder was slightly elevated compared to the gas only and zeolite systems. At $P \geq 100$ W, k_f (N_2) decreased in the presence of a zeolite pellet. At $P < 100$ W, k_f (NO) for a given system is higher compared to the N_2 rate constants. Additionally, k_f (NO) values demonstrate little to no dependence on the addition of a material. As detailed in the Methods section and depicted in Figure S1, after reaching a maximum, the intensity of NO follows an exponential decay to a steady state, denoted as k_d. Due to low signal-to-noise ratios at 25 W, k_d (NO) values are not reported. k_d (NO) values demonstrated a slight dependence on P; however, several conditions are within the experimental error of each other.

https://dx.doi.org/10.1021/acscatal.0c00794
ACS Catal. 2020, 10, 6546−6560

Table 1. k_f (s^{-1}) Values in N_2O Plasma Systems[a]

plasma	P (W)	gas only	Pt powder	zeolite
N_2	25	1.551 (0.912)	2.431 (0.332)	1.484 (0.0432)
	50	2.269 (0.195)	4.438 (0.757)	2.925 (0.0523)
	75	4.778 (0.0703)	6.291 (0.460)	4.310 (0.132)
	100	7.264 (0.216)	9.444 (0.381)	5.713 (0.173)
	125	11.845 (0.908)	12.700 (0.889)	9.770 (0.0961)
	150	14.260 (0.803)	17.579 (2.360)	12.171 (0.522)
NO	25	3.249 (0.240)	4.596 (0.478)	3.622 (0.604)
	50	4.933 (0.548)	6.347 (1.586)	6.069 (0.750)
	75	6.273 (1.327)	7.589 (0.540)	7.496 (1.284)
	100	6.625 (0.813)	9.193 (0.833)	10.930 (0.807)
	125	11.362 (1.669)	11.315 (1.741)	13.345 (0.899)
	150	14.229 (2.550)	16.326 (3.714)	14.145 (2.454)

[a]Values in parentheses represent standard deviation calculated from the mean of $n \geq 6$ trials.

Table 2. k_d (s^{-1}) Values in N_2O Plasma Systems[a]

plasma	P (W)	gas only	Pt powder	zeolite
NO	50	4.105 (1.056)	2.780 (0.628)	1.539 (0.459)
	75	6.445 (1.055)	2.937 (1.163)	4.408 (0.888)
	100	7.717 (0.739)	6.038 (1.871)	4.632 (0.545)
	125	11.843 (1.234)	6.533 (0.989)	6.406 (0.343)
	150	9.300 (1.015)	7.289 (0.865)	8.243 (1.146)

[a]Values in parentheses represent standard deviation calculated from the mean of $n \geq 6$ trials.

Evaluation of plasma kinetics can provide insights into plasma ignition and initial plasma−catalyst interactions; however, illumination of steady-state energetics is also a critical component of a holistic evaluation of PAC systems.

T_R values of excited-state N_2 and NO are plotted as a function of applied rf power and catalyst, Figure 6a,b, respectively and included in Table 3. When no material is present, T_R (N_2) values have thermalized to approximately room temperature, with little to no power dependence. The Pt foil system shows a slightly stronger power dependence, T_R (N_2) increases to 340 ± 10 K at P = 175 W. Interestingly, the two porous materials impact the ability of N_2 molecules to rotationally thermalize, particularly the Pt powder catalysts as T_R (N_2) = 405 ± 10 K at P = 175 W. However, this increase in T_R (N_2) values as power increases is significantly smaller compared to the increase in T_R (NO) values, shown in Figure 6b. A positive correlation between rf P and T_R (NO) was determined, where T_R (NO) values increased by ∼300 K as P increased from 25 to 175 for each system. At 150 W, the addition of a catalyst (Pt foil and power, zeolite pellet) resulted in increased T_R (NO) values, yet T_R (NO) values converge within the experimental error as P increases to 175 W.

T_V values for excited-state N_2 and NO are listed in Table 4. Regardless of the catalyst, T_V (N_2) increases as a function of rf power. T_V (NO) also displays power dependence; however, the increase in T_V (NO) between 25 and 175 W is significantly less compared to that observed for N_2 species. When no material is present, T_V (NO) values at lower P (25−100 W) are all within the experimental error of each other. As the rf power is increased from 100 to 175 W, an increase in T_V (NO) is observed. Detailed in the Methods section, ΔT_V for N_2 (Figure 7a) and NO (Figure 7b) was measured as a function of power and material to probe differences in vibrational energy partitioning upon the addition of a catalyst. At all conditions

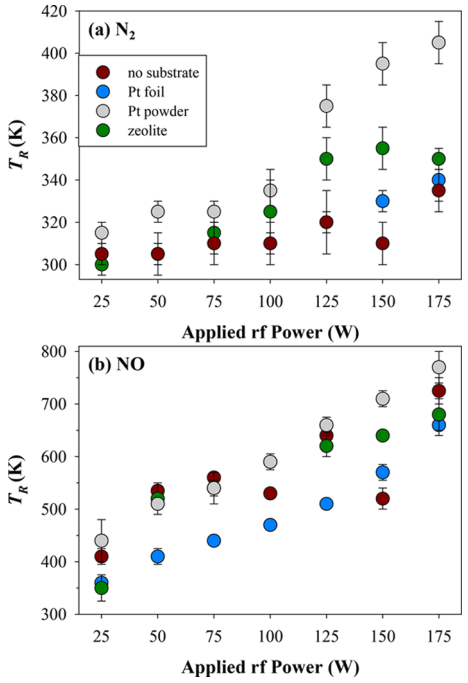

Figure 6. T_R (K) values for (a) N_2 and (b) NO molecules, plotted as a function of applied rf power and material within p = 100 mTorr N_2O discharge. Error bars represent one standard deviation from the mean ($n \geq 3$).

Table 3. T_R (K) for Excited-State N_2 and NO within N_2O Plasmas[a]

plasma	P (W)	gas only	Pt foil	Pt powder	zeolite
N_2	25	305 (5)	305 (5)	315 (5)	300 (5)
	50[b]	305 (10)	305 (5)	325 (5)	305 (5)
	75	310 (10)	310 (5)	325 (5)	315 (5)
	100[b]	310 (5)	310 (10)	335 (10)	325 (15)
	125	320 (15)	320 (5)	375 (10)	350 (10)
	150[b]	310 (10)	330 (5)	395 (10)	355 (10)
	175	335 (10)	340 (10)	405 (10)	350 (5)
NO	25	410 (15)	360 (10)	440 (40)	350 (25)
	50[b]	535 (10)	410 (15)	510 (10)	520 (30)
	75	560 (10)	440 (10)	540 (15)	540 (30)
	100[b]	530 (5)	470 (10)	590 (15)	590 (10)
	125	640 (10)	510 (10)	660 (15)	620 (20)
	150[b]	520 (20)	570 (15)	710 (15)	640 (10)
	175	725 (25)	660 (20)	770 (30)	680 (30)

[a]Values in parentheses represent standard deviation calculated from the mean of $n \geq 3$ trials. [b]Previously reported.[28]

herein, vibrational cooling of N_2 molecules, as measured by ΔT_V, was observed upon the addition of catalysts. At 25 and 50 W, vibrational cooling was relatively independent of the catalyst type; however, as P is increased to 175 W, the temperature difference between the Pt powder and material-free system became more pronounced [ΔT_V (N_2) = −2700 ± 210 K]. ΔT_V with zeolite and Pt foil catalysts displays a similar, limited dependence on P [ΔT_V (N_2) ≤ − 500 K] below P = 125 W. Notably, ΔT_V at 150 and 175 W is significantly larger (−1170 ± 60 and − 990 ± 90 K, respectively) in the presence of a zeolite pellet. Unlike T_V (N_2), vibrational cooling of NO was not observed for all materials, shown in Figure 7b and Table 4. At 25 W, the presence of catalysts does not impact the resulting NO vibrational energetics. As P is increased in the

https://dx.doi.org/10.1021/acscatal.0c00794
ACS Catal. 2020, 10, 6546−6560

Table 4. T_V (K) for Excited-State N_2 and NO within N_2O Plasmas[a]

plasma	P (W)	gas only	Pt foil	Pt powder	zeolite
N_2	25	2850 (15)	2500 (20)	2560 (180)	2570 (70)
	50	3450 (80)	3150 (15)	2960 (100)	3010 (160)
	75	3880 (70)	3670 (70)	3380 (70)	3700 (40)
	100	4410 (50)	4150 (15)	3650 (30)	4060 (90)
	125	5290 (90)	4600 (10)	3990 (60)	4830 (10)
	150	6360 (50)	5050 (30)	4210 (70)	5190 (40)
	175	6890 (50)	6380 (70)	4190 (210)	5900 (80)
NO	25	2880 (20)	2760 (20)	2990 (10)	2850 (140)
	50[b]	2870 (60)	2770 (20)	2900 (50)	3300 (160)
	75	2910 (90)	2790 (10)	2910 (20)	3320 (120)
	100[b]	2900 (10)	2780 (20)	2860 (40)	3630 (100)
	125	3080 (50)	2920 (130)	2910 (20)	3550 (120)
	150[b]	3300 (170)	2860 (10)	3160 (50)	4200 (180)
	175	3850 (110)	3500 (30)	3730 (90)	4050 (140)

[a]Values in parentheses represent standard deviation calculated from the mean of $n \geq 3$ trials. [b]Previously reported.[28]

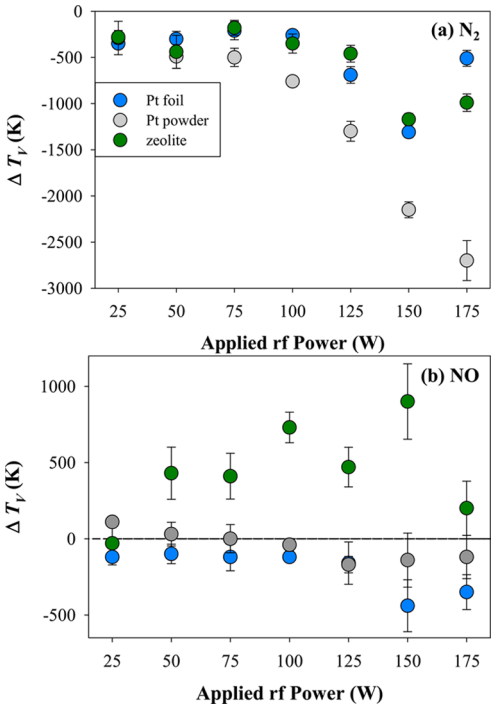

Figure 7. ΔT_V for (a) N_2 and (b) NO as a function of applied power and material within a 100 mTorr N_2O discharge.

zeolite system, T_V (NO) is enhanced, with limited P dependence. The two Pt materials studied here do not have a substantial impact on T_V (NO). Indeed, many of the data points calculated here are within the experimental error of the gas only system. The relative species density, energy partitioning, and kinetic distributions have been measured as a function of the operating conditions and catalytic material within single-stage PAC systems. Noted in the Introduction, the configuration of the plasma and catalyst may also impact the efficacy of PAC technologies.

Figure 8 depicts $[N_2]$, [O], and [NO] density as a function of P and plasma−catalysis configuration for the Pt powder materials. For comparison, gas only and single-stage actinometric data are shown in Figure 3. At 25 and 50 W, plasma catalysis orientation does not impact $[N_2]$. As P increases from 75 to 175 W, $[N_2]$ decreases, with little difference between the

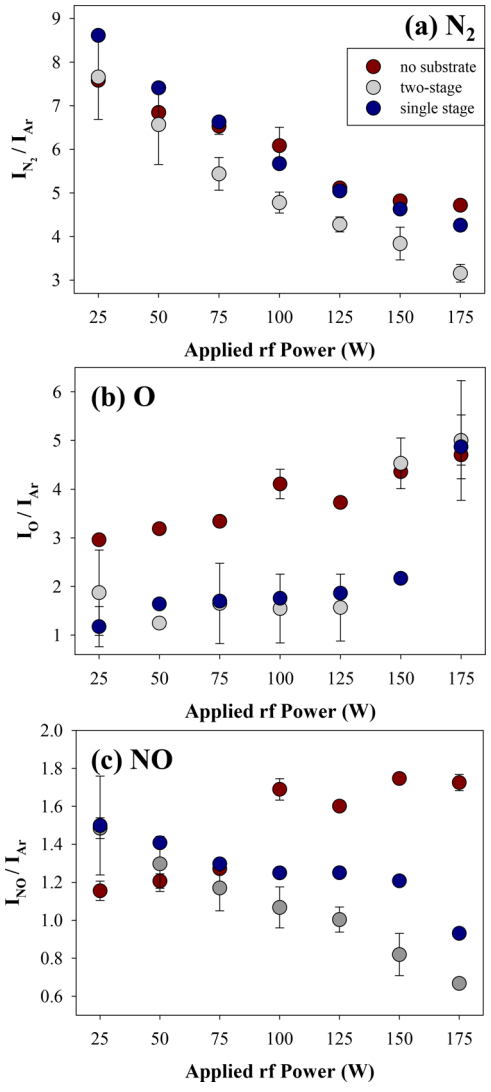

Figure 8. Species density as a function of P and plasma catalysis setup, with Pt powder catalysts present. Error bars represent one standard deviation from the mean (n = 4).

gas only and single-stage configuration. Additional decreases in $[N_2]$ are observed, however, with the two-stage system. Described above, [O] slightly increases with P when no

https://dx.doi.org/10.1021/acscatal.0c00794
ACS Catal. 2020, 10, 6546−6560

material is present. At P < 125 W, less atomic O is formed, with no dependence on single- or two-stage configuration. At 175 W, [O] has no apparent dependence on PAC orientation. [NO] decreases substantially at higher P with the addition of Pt nanopowder in the coil region of the plasma and was further diminished in the pre-plasma catalysis orientation.

To better understand these gas-phase trends and to understand the impact of plasma processing on each material, the catalysts were studied before and after plasma exposure. PXRD and XPS techniques were used to characterize bulk and surface properties, respectively. The diffraction patterns of Pt foil (Figure S4a) and powder (Figure S4b) are shown for untreated as well as N_2O plasma-treated materials. The diffraction peaks at 2θ = 39.6, 46.4, and 67.4° in Figure S3a,b correspond to the reflections (111), (200), (220), respectively, consistent with the face-centered cubic (fcc) structure of platinum.[35] The (111) diffraction peak of Pt foil has nominally disappeared after a 175 W plasma treatment, indicative of material damage after N_2O plasma exposure. The Pt foil used herein was 0.025 mm thick; therefore, it is likely that energetic plasma species impacted the overall bulk crystallinity of this material. The measured (200) and (220) diffraction peaks are nominally unchanged for Pt foil materials; no substantive changes to the XRD patterns were measured for the Pt nanopowder. The inset EDS image in Figure S4b corresponds to Pt powder after exposure to a 100 mTorr, 175 W N_2O plasma for 10 min, revealing that the bulk of the material is composed of platinum, with some oxygen dispersed throughout the material. These data, in conjunction with the PXRD diffraction, highlight that the bulk chemistry of these materials is metallic Pt. In XPS spectra, both Pt foil and Pt powder (Figure 9a,b, respectively) show the addition of a peak at 78.0 eV in the Pt_{4f} spectra, corresponding to the oxidation of the Pt catalyst.

Atomic compositions for these materials are reported in Table 5. Both Pt materials were used as received and had high concentrations of carbon on the surface. Post plasma exposure at either 25 or 175 W, the amount of oxygen on the Pt foil surface increased compared to the untreated material, with a concomitant decrease in carbon. In some spots on the Pt powder materials, no carbon was detected in the survey spectra; hence, there is a large error associated with the amount of carbon adsorbed to the surface of the nanopowder. In contrast to Pt foil, after gas and plasma exposure, the carbon content on Pt powder increased significantly. Although the bulk of these materials are metallic Pt, verified through PXRD and EDS, the surface chemistry is much more complex and clearly affected by plasma exposure. These data exemplify the need for robust material characterization (e.g., bulk and surface properties) in conjunction with gas-phase studies.

The impact of plasma−catalyst configuration on gas-phase species densities was also investigated with a zeolite pellet as the catalyst (Figure 10). N_2 density decreases as a function of P for the two-stage and gas only systems, converging to the same values at $P \geq 75$ W. The single-stage system resulted in significantly less atomic O compared to both the gas only and two-stage systems studied herein, with largely no dependence on P. At 175 W, there is substantially more O produced in the two-stage system, and a slight decrease in [NO] was detected with this configuration. At $P \leq 125$ W, the two-stage zeolite system produced more NO in the discharge compared to when no catalyst is present, whereas a zeolite placed directly in the discharge enhanced the decomposition of NO at higher power.

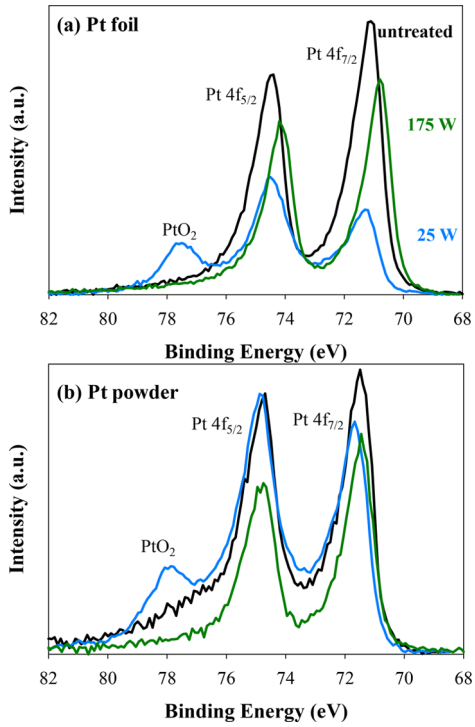

Figure 9. High-resolution Pt 4f XPS spectra for untreated Pt (a) foil and (b) powder (black traces) and N_2O plasma-treated materials at P = 25 W (blue traces) and 175 W (green traces), with p = 100 mTorr and t = 10 min.

The surface and bulk properties of the zeolite materials were also characterized after these plasma exposures. XPS atomic composition is listed in Table 5, and Figure 11 shows the high-resolution Si_{2p} and O_{1s} XPS spectra for untreated (a,d), single-stage (b,e), and two-stage (c,f) N_2O plasma-exposed zeolite pellets. Small amounts of Na (<1%) were detected in the XPS survey scan; however, high-resolution Na_{1s} spectra were not collected because of the signal (see Methods section). The high-resolution Si^{2p} spectra show two Si binding environments: Si(−O_4) at 103.4 eV and Si(−O_3) at 102.8 eV.[36] The primary oxygen binding environments include the Si−O−Si band at 531.7 eV and Si−O−Al band at 530.8 eV.[31,37] The single-stage system depicts an increase in the Si(−O_4) (Figure 11b) and Si−O−Al (Figure 11e) binding environments compared to the untreated or two-stage system.

This suggests that some surface "cleaning" occurs to expose the underlying aluminosilicate bridges. Although there are slight differences in the surface chemistry of zeolite materials after plasma processing, material morphology and bulk properties remained largely unchanged (Figure S6). To further investigate the potential removal of surface contaminants, the surface chemistry of oven-calcinated zeolite pellets was assessed with XPS before and after N_2O plasma exposure (p = 100 mTorr P = 175 W, t = 10 min) (Figure S7). The Si−O−Al binding environment increased when the zeolite was surface-cleaned with oven exposure, likely as a result of removal of adventitious surface carbon to reveal the underlying aluminosilicate material. This binding environment became more prevalent after N_2O plasma exposure, further supporting the creation of oxygen vacancies on the surface via surface cleaning and removal of surface carbon.

https://dx.doi.org/10.1021/acscatal.0c00794
ACS Catal. 2020, 10, 6546−6560

Table 5. XPS Atomic Composition for Pt and Zeolite Materials[a,b]

	Pt foil			Pt powder				zeolite pellet		
atom	UT	25 W	175 W	UT	gas[c]	25 W	175 W	UT[c]	gas[d]	175 W
Pt (%)	25.3 (1.9)	23.8 (2.2)	26.0 (2.9)	53.4 (12.2)	32.3 (6.8)	32.5 (2.0)	29.6 (2.1)			
O (%)	18.3 (2.6)	53.5 (2.5)	39.1 (6.2)	37.0 (4.1)	29.1 (0.8)	45.5 (4.2)	31.6 (4.2)	57.5 (4.0)	57.3 (1.2)	60.3 (3.5)
C (%)	56.3 (3.6)	22.7 (3.0)	34.9 (4.1)	9.5 (13.6)	38.6 (6.7)	22.0 (4.6)	38.8 (7.1)	22.7 (7.0)	21.2 (0.9)	14.4 (5.9)
Si (%)								15.5 (2.6)	15.7 (0.8)	20.9 (2.2)
Al (%)								4.4 (0.6)	5.7 (0.4)	4.4 (0.4)

[a]Values in parentheses represent one standard deviation for the measurement. [b]Treatment conditions: p = 100 mTorr, t = 10 min. [c]Materials were placed in a pre-plasma catalysis chamber. [d]Previously reported.[31]

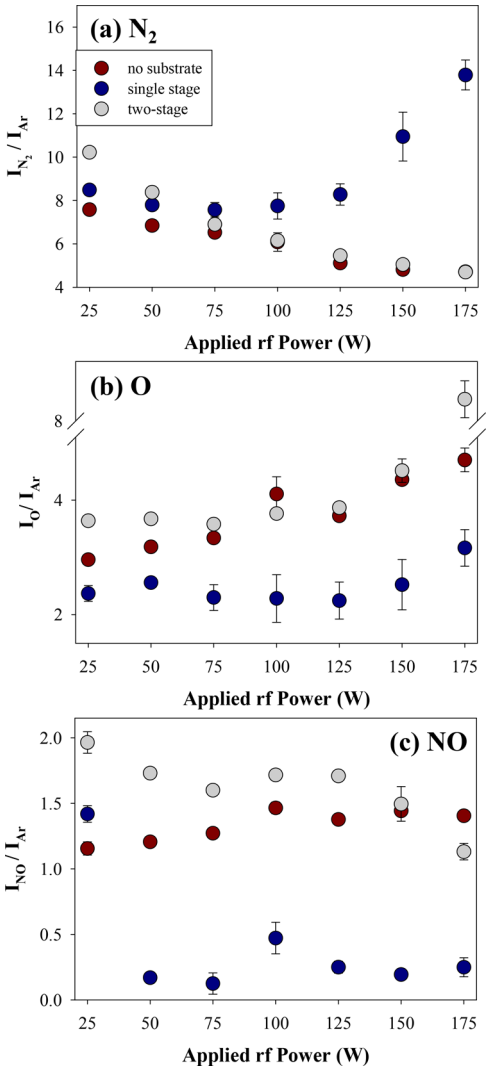

Figure 10. Species relative density as a function of P and plasma catalysis setup, with zeolite pellets present. Error bars represent one standard deviation from the mean (n = 4).

4. DISCUSSION

Detailed in the Introduction, the applicability of PAC for decomposition of pollutants is inherently hindered by a lack of knowledge regarding plasma−catalyst interactions. This pertains to both the potential modification of the catalyst by the plasma and the ability of the material to influence plasma chemistry. Therefore, a holistic experimental approach is necessary to understand relationships between gas-phase species, processes at the gas−surface interface, and resulting catalyst properties. For example, within plasmas (sans catalyst), N_2O is hypothesized to decompose primarily through multiple-electron impact dissociation pathways, described briefly in reactions 5 and 6.[38]

$$N_2O_{(g)} + e^- \rightarrow N_{2(g)} + O_{(g)} + e^- \quad (5)$$

$$N_2O_{(g)} + e^- \rightarrow N_{(g)} + NO_{(g)} + e^- \quad (6)$$

Using inert-gas actinometry, the relative density of these reaction products can be elucidated as a function of operating conditions. With no material in the plasma discharge, [NO] slightly increases as P increases from 25 to 175 W. This could indicate further fragmentation of the precursor (N_2O) at higher power, or NO could form via additional reactions between O and N. This study sought to abate N_2O via PAC; however, the decomposition of N_2O to NO (reaction 6) is non-ideal as reactions between NO and other environmental byproducts can be detrimental to the atmosphere. Given this type of complexity, the data presented here reveal several major observations regarding the interactions of catalysts with N_2O plasmas.

The first major observation is that the presence of a zeolite pellet dramatically changes the plasma chemistry, ultimately increasing the decomposition of N_2O (and NO) into benign N_2 at rf $P \geq 75$ W (Figure 3). Consequently, this sharp decrease in NO in the presence of a zeolite pellet coincides with a sharp increase in N_2 (Figure 3a), expressed via reaction 7[25]

$$NO_{(g)} + N_{(g)} \rightarrow N_{2(g)} + O_{(g)} \quad (7)$$

Atomic nitrogen emission peaks are not observed in the N_2O emission spectra, further supporting its consumption in reaction 7 to form N_2 and O species. Generally, N_2O and subsequent NO decomposition increased by increasing the applied rf P for both Pt powder and zeolite materials. This likely occurs as a result of more reactive species being generated at a higher power. Upon plasma ignition, a variety of reactive species are created via excitation, ionization, and dissociation, including excited-state N_2, N radicals, and N_2^+ ions. Jo et al. hypothesize that these species nominally decompose N_2O via reaction 8.[12]

$$N_2(A^3\Sigma_u^+)_{(g)} + N_2O_{(g)} \rightarrow 2N_{2(g)} + O_{(g)} \quad (8)$$

At 25 W, [NO] in the discharge increased upon the addition of a catalyst, suggesting that a gas-phase molecule could remove adsorbed O from the surface and undergo reactions to form additional NO. Within the Pt foil system, [NO] is elevated compared to the gas only system at $P \leq 75$ W, but as power increases to 175 W, these systems are the same within the experimental error. Pt foil seems to have little to no impact on the plasma environment; the densities of N_2, NO, and OH

https://dx.doi.org/10.1021/acscatal.0c00794
ACS Catal. 2020, 10, 6546−6560

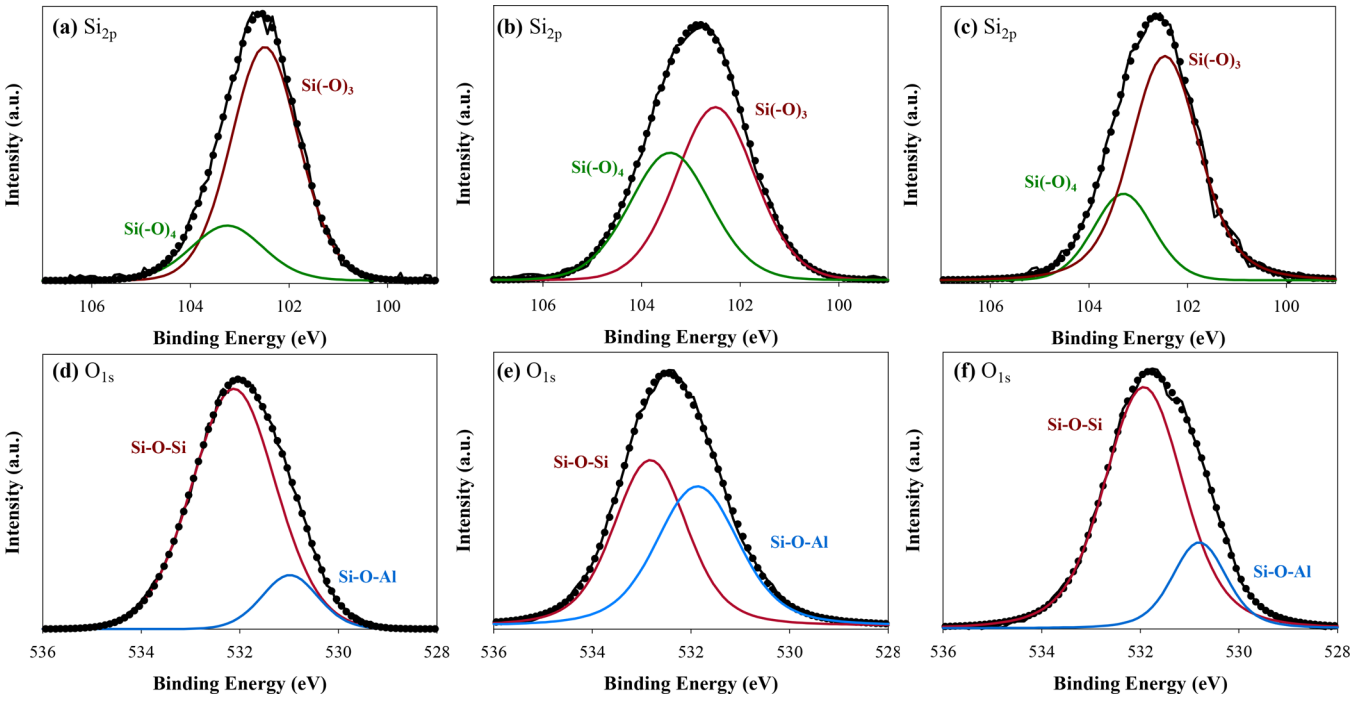

Figure 11. High-resolution Si_{2p} (top) and O_{1s} (bottom) XPS spectra for (a,d) untreated, (b,e) single-stage, and (c,f) two-stage N_2O plasma-treated zeolite pellets (100 mTorr, 175 W, 10 min).

are within the experimental error with the gas only system at most rf powers studied here. Depicted in Figure 3b, both Pt powder and zeolite materials drastically altered the plasma chemistry, ultimately decreasing the amount of NO in the discharge at $P \geq 50$ W (zeolite) and $P \geq 100$ W (Pt powder). Therefore, it is likely that the porous network of these materials impacts the ability of the catalyst to decompose N_2O and NO. Illustrated in Figure 2, pore size and shape drastically differ between the Pt nanopowder and microstructured zeolite. The variability of the porous network could impact the formation of microplasmas within the pores of the catalyst, which is hypothesized to enhance pollutant decomposition.[39]

Zhang et al. studied the influence of the material dielectric constant on plasma generation inside catalyst pores using a two-dimensional fluid model of an atmospheric pressure helium discharge.[40] The authors concluded that pore size and shape are a crucial variable in the propagation of plasma into catalyst pores. In a 100 μm pore, the electron impact ionization in the pore is greatly enhanced for dielectric constants (ε_r) below 300; however, ferroelectric materials with dielectric constants above 300 did not yield plasma enhancement inside catalyst pores, regardless of pore size. The authors argue common catalyst supports [Al_2O_3 (ε_r = 8−11), SiO_2 (ε_r = 4.2), and zeolites (ε_r = 1.5−5)] should more easily allow formation of microdischarges within pores, even those of smaller sizes.[40] Aluminosilicate zeolites have a smaller dielectric constant compared to Pt (ε_r = 6.5−7.5), and the zeolites employed in this study have significantly larger pores compared to the nanostructured Pt powder. This suggests that microdischarges may form more easily with the zeolite catalyst; hence, it is the system with the highest degree of NO decomposition. As evidenced by the results depicted in Figure 3, chemical nature and morphology (i.e., pore size) can have a substantial impact on the resulting plasma composition. An additional variable is the catalyst placement, which is why the PAC community is actively investigating different plasma−catalyst configurations for pollution abatement, including those where the plasma and catalyst can directly interact (single-stage) or be separated (two-stage).[19] By exploring both single- and two-stage arrangements, synergisms between gas−catalyst (two-stage) and plasma−catalyst (single-stage) can be separately evaluated.

Within a two-stage, pre-plasma catalysis configuration, gas flows over the catalyst and is further treated by the inductively coupled plasma (Figure 1b). As the porous materials (Pt powder and zeolites) had the greatest impact on the amount of NO in the discharge (Figure 3b), they were chosen for the two-stage studies. As noted above, [NO] decreases substantially at higher powers ($P \geq 100$ W) with the addition of a nanostructured Pt catalyst in the discharge. Thus, a second major observation herein was the further diminished NO density in the system with the pre-plasma catalysis setup compared to the gas only and single-stage configurations (Figure 8c). Within the two-stage system, $N_2O_{(g)}$ likely interacts with the catalyst via reactions 1 and 2, wherein the interactions with adsorbed O are hypothesized to be the rate-limiting step.[12] Density functional theory (DFT) studies have shown that $N_2O_{(g)}$ can be easily absorbed on metal surfaces, calculating a negative adsorption energy of N_2O on the top site of Pt(111) surfaces.[41] Using CaS(100) as a catalyst in DFT calculations, Wu et al. computed a 1.228 eV energy requirement for N_2O to decompose to $N_{2(g)}$ and $O_{(ads)}$ (reaction 1). The subsequent removal of $O_{(ads)}$ from the surface is more energy-intensive, discussed further below.[42] At low temperatures, there is limited regeneration of active sites due to adsorbed species; hence, overall catalytic activity is diminished. In a review article, Konsolakis compiled literature studies of N_2O decomposition on bare oxides, where system temperatures ranged from 300 to 710 °C.[43] In the present study, all results were nominally collected at room temperature, suggesting that the combination of the catalyst with a plasma inherently removes the necessity for high reaction

https://dx.doi.org/10.1021/acscatal.0c00794
ACS Catal. 2020, 10, 6546−6560

temperatures. Within the single-stage discharge, N_2O is mostly fragmented upon ignition (reactions 5 and 6); therefore, it is unlikely that intact N_2O is interacting with the material.

To further probe the differences in these reactor configurations and resulting plasma chemistry, the catalysts were thoroughly characterized before and after plasma exposure. Specifically, PXRD and XPS techniques were used to characterize bulk and surface properties of the materials, respectively. Both Pt catalysts were used as received and contained large amounts of adventitious carbon on the surface. The high experimental error reported for the untreated Pt powder (Table 5) resulted from some sampling locations on the surface containing no measurable carbon. As detailed in the Methods section, a minimum of three spots on three samples was analyzed for XPS studies to gain a representative view of the surface chemistry. A series of cleaning strategies were explored to remove surface contaminates from Pt foil and nanopowder, detailed in the Supporting Information. Briefly, O_2 plasmas are often utilized to remove surface contaminants through etching mechanisms; however, Pt foil became oxidized after 100 mTorr, 100 W, 5 min O_2 plasma treatment, shown in Figure S5. Additionally, Pt foil samples were sonicated in 200 proof ethanol (EtOH) for 30 min, which also significantly altered the Pt surface chemistry compared to the as-received material, illustrated in Figure S5. Additional fabrication methods were explored for the Pt nanopowder to create materials suitable for a vacuum environment. First, Pt nanopowder slurries were created with either EtOH or hexane, and these were drop-cast onto glass slides, as described previously.[44] Using XPS to investigate the surface of fabricated Pt materials, the addition of the PtO_2 peak within the high-resolution Pt_{4f} XPS spectra was measured in samples drop-cast with EtOH. Pt nanopowder samples prepared with hexane resulted in poor adhesion and detection of the underlying glass (SiO_2) support in some samples. Second, Pt nanopowder was exposed to UV light for 10 min to remove surface contaminants. This was, however, largely unsuccessful because of the significant amount of C measured on the surface [28.0 (4.5)%]. These data are documented in Table S1. Ultimately, as described in the Methods section, Pt foil was used as-received, and the Pt nanopowder was secured to glass slides via double-sided C tape.

Although the presence of carbon species may impact gas−surface reactions in these systems and limit accessibility to catalytic sites on the surface of the Pt materials, our results document a substantial decrease in $NO_{(g)}$ with Pt nanopowder materials in both plasma−catalyst configurations studied here. Within the two-stage configuration, flowing 100 mTorr N_2O over the Pt powder material for 10 min does not appear to change the catalyst (Table 5), whereas placing the Pt catalysts in the discharge actively changes the chemical identity of the catalysts and hence may hinder catalytic activity. Both Pt materials are clearly modified upon plasma exposure, as an additional binding environment at 75.0 eV, corresponding to PtO_2, which appears in the Pt_{4f} XPS spectra (Figure 9). Several studies have demonstrated that an increase in oxygen negatively influences the ability of Pt to decompose N_2O.[9,12] Surface oxygen on the Pt powder is likely blocking the active sites of the catalyst; hence, [NO] is lower in the two-stage system compared to the single-stage configuration.

A two-stage PAC system was also investigated using a zeolite pellet (Figure 10). For both the gas only and two-stage systems, [N_2] decreases as rf P increases from 25 to 175 W. The single-stage system resulted in significantly less O compared to both the gas only and two-stage system, with largely no dependence on rf power. Within the two-stage system at P = 25−125 W, there is more NO in the gas phase compared to when no catalyst is present. This suggests that the decomposition of the N_2O precursor into N_2, NO, and O is occurring, yet further NO decomposition is not. Clearly, in the case of zeolites, a single-stage system is optimal, exemplified in Figure 10c. The distinct and exaggerated decrease in NO indicates that the plasma is necessary for activation of the catalyst. Furthermore, plasma exposure does not appreciably change the surface or bulk chemistries of the zeolite materials; therefore, the catalyst is not being degraded or damaged by the plasma (Figure S6 and Table 5). These gas-phase and material characterization results support the hypotheses proposed in the Introduction, namely, affordable materials (e.g., zeolites) can be utilized in PAC pollution abatement.

As noted in the Introduction, it is imperative to study both the steady-state plasma and discharge phenomena as a function of time to obtain a comprehensive representation of plasma−surface interactions. As such, TR-OES was used to probe the sharp decrease of [NO] in the single-stage, zeolite system. Shown in Figure 4b, [NO] suddenly decreases 10 s after plasma ignition at P = 150 W. Small amounts of Ar (∼10%) were added to the system for actinometric purposes, which could also influence the decomposition and formation of plasma species. Lee and Kim found out that the application of an Ar plasma in conjunction with alumina-supported Ru catalysts could decompose N_2O bonds to form NO, N, and O species at relatively low material temperatures.[45] Using a 245 °C reaction temperature, the authors noted that as the N_2O/Ar ratio increased to 3:1, N_2O conversion decreased to 23.8%.[45] These data suggest that Ar plays an important role in the dissociation of N_2O. As the atmosphere contains <1% Ar, we sought to study plasma kinetics and energetics without the addition of Ar, quantifying rate constants for formation and destruction as a function of plasma operating P and catalysts.

Through TR-OES, the formation profiles of excited-state N_2 and NO within an N_2O discharge were measured and differentiated. The intensity of N_2 (337.0 nm) increases as a function of time, ultimately reaching an apparent steady state, where NO emission (235.9 nm) initially increases to a local maximum and subsequently decays. These data suggest that reactions 6 and 7 are occurring sequentially in the discharge: NO is initially formed through the dissociation of the N_2O precursor, and then, a decline in NO intensity is observed as it undergoes further reactions within the plasma. When no material is present, the discharge operating mode impacts k_f values. Specifically, when the discharge shifts from inductance (E) to capacitance (H) mode operation at 125 and 150 W, there is an increase in both k_f (N_2) and k_f (NO) values.

Additionally, at P > 100 W, k_f (N_2) decreased in the presence of a zeolite pellet, where k_d (NO) appears largely independent of the catalyst. As described above, we hypothesize that the structure and surface chemistry of the zeolite pellet promote formation of microdischarges near or within the pores of the material. Consequently, the formation of N_2 species within the bulk discharge could be impacted by the microdischarges within the material. Collisional quenching of excited-state N_2 is another proposed pathway for decreased rate constants at certain conditions. We have previously studied the impact of zeolite catalysts within a 100% N_2 plasma, where a decay to steady-state emission (similar to

https://dx.doi.org/10.1021/acscatal.0c00794
ACS Catal. 2020, 10, 6546−6560

the NO within N_2O herein) was documented at 125 and 150 W with zeolite(s) present.[31] Furthermore, the addition of a single zeolite pellet in the coil region of the reactor decreased T_V (N_2) at $P \geq 75$ W. Upon increasing the amount of zeolite in the system via lining the reactor shown in Figure 1a with zeolite pellets, enhanced N_2 vibrational cooling was measured at all applied rf powers studied.[31] To further assess these hypotheses of plasma−material interactions in a more environmentally relevant plasma system, a third major finding herein was the deciphering of energy partitioning between degrees of freedom and across multiple molecules (i.e., N_2 and NO) formed in N_2O plasmas.

Excited-state N_2 and NO T_R values were determined as a function of rf power and catalyst (Figures 6a,b). The Pt powder system had the most significant impact on T_R (N_2) values compared to the material-free discharge. As shown in Figure 6a and Table 3, it appears that the discharge mode and resulting rotational distributions are interrelated with Pt nanopowder present. T_R (N_2) values increase from 335 ± 10 K (100 W) to 375 ± 10 K (125 W) as the discharge shifts from E- to H-mode operation. This trend is not prevalent in the zeolite system, T_R (N_2) values at P = 100 W and 125 W are within the experimental error, although T_R generally increases within increasing rf power. Rotational energy distributions of absorbing and emitting N_2 molecules in a variety of discharges (e.g., N_2, N_2O, N_2/O_2) have been previously studied via broadband absorption spectroscopy (BAS) and OES, respectively, where all T_R (N_2) values were less than 440 K.[28] This suggests that the rotational populations within N_2 molecules readily thermalize to slightly above room temperature, an observation that holds here, as all calculated T_R (N_2) values are less than 405 K (Figure 6a). Rotational temperatures for excited-state NO radicals are significantly elevated compared to N_2. When no material is present, as P increases from 25 to 175 W, T_R (NO) increases from ∼400 to ∼725 K. This is not, however, a clear, linear increase as T_R (NO) at 50 and 150 W are within the error. At P = 50−125 W, a decrease in T_R (NO) of approximately 50−130 K was measured in the presence of Pt foil. This suggests that excited-state molecules interact with flat Pt foil and scatter with some rotational relaxation at these powers. At 150 W, an increase in T_R (NO) is determined for all catalysts, with Pt powder yielding the highest T_R value (710 K) followed by the zeolite (640 K), Pt foil (570 K), and gas only (520 K) systems. These data suggest that material morphology may play a more important role in plasma energetics than material chemistry; the porous materials impact the ability of NO molecules to thermalize rotationally. At the highest power studied (175 W), T_R does not display a strong dependence on the catalysts even though there is a large difference in the amount of NO in the discharge with no material ([NO] = 1.73 ± 0.04) compared to when a zeolite pellet is present ([NO] = 0.25 ± 0.07). Rotational relaxation is a relatively fast process, typically requiring fewer than ten collisions to reach equilibrium. Therefore, on the timescale that both the energetic and actinometric data were collected (i.e., minutes), the NO ($A^2\Sigma^+$) radicals have effectively reached a quasi-rotational equilibrium and material effects are negligible, regardless of the amount of NO in the discharge. All T_R reported herein are <800 K, an order of magnitude less than the T_V values for excited-state N_2 and NO, listed in Table 4.

Regardless of the material, as applied rf power in the system is increased from 25 to 175 W, there is a clear increase in T_V (N_2), a trend we have previously quantified in N_2 (with and without catalysts),[31] NO (gas only),[30] and N_2/O_2 (gas only)[28] rf ICPs. At all power conditions studied herein, a decrease in T_V (N_2) was determined upon the addition of catalysts, where the temperature difference between the Pt powder and material-free system increased with increasing power. The discharge mode of the plasma likely contributes to the enhanced vibrational cooling documented in Figure 7a; as P increases from 125 to 150 W, the rf plasma shifts from E-mode (low plasma density) to H-mode (higher plasma density). We have previously studied T_V (N_2) within a 100% N_2 plasma, with TiO_2 and zeolite materials in the discharge, and a similar decrease in T_V with catalysts present was measured.[31] N_2 vibrational energy distributions within N_xO_y plasmas are clearly impacted by a catalyst; therefore, examining the plasma−material interface could garner additional insights into these phenomena.

Larsson described a selective energy transfer (SET) model to explain catalyst−reactant interactions,[46−48] where the catalyst provides the energy required to populate higher vibrational levels within a molecule. This model suggests that vibrationally excited N_2 molecules can interact with a material and scatter with some energy loss, potentially through an energy transfer mechanism.[49] Larsson investigated numerous catalytic systems [e.g., hydrocarbon cracking over zeolites[50] and ethane hydrogenolysis over Pt, Ni, Fe, and Co catalysts[51]], applying the SET model to probe vibrational resonance processes. In many of the SET systems reported in the literature, little chemisorption of the intact molecule onto the catalyst surface is observed, depending on the catalyst.[47] Therefore, we sought to understand the plasma−material interactions within N_2O discharges using a SET model. Pt nanopowder was exposed to a P = 175 W N_2O plasma for 10 min, as depicted in Figure 9b; the resulting Pt_{4f} XPS spectra did not exhibit the additional PtO_2 peak, documented at P = 25 W. Furthermore, at P = 175 W, the most pronounced decrease in T_V (N_2) values was measured, whereas at P = 25 W, limited vibrational cooling was measured. The combination of these gas-phase and surface chemistry data suggest that at P = 175 W, a vibrational energy transfer is occurring with a Pt powder catalyst.

Unlike T_V (N_2) values, vibrational cooling of NO did not occur for all catalysts studied herein (Figure 7b and Table 4). With a zeolite, as power increases, T_V (NO) values also increase. Examining ΔT_V (NO) (Figure 7b) reveals that the zeolite clearly has a very different effect on plasma energetics compared to the Pt materials. As the applied power is increased, only the zeolite system displays an enhancement in T_V (NO). Interestingly, neither of the Pt materials have a substantial impact on the energetics of NO radicals in the discharge. There are fewer NO and N_2 molecules in the discharge when a Pt powder catalyst is present in the discharge from 100−175 W, as well as enhanced N_2 vibrational cooling (Figure 7a). The lack of vibrationally excited N_2 under these conditions suggests that N_2 molecules with significantly high T_V are likely involved in additional gas-phase reactions to form $NO_{(g)}$, $O_{(g)}$, and $OH_{(g)}$. Note, all data showed herein correspond to excited-state, emitting gas-phase species. We have previously reported vast differences in vibrational temperatures of excited- and ground-state molecules; therefore, it will be essential to probe the ground-state species in these N_2O-catalyst systems via BAS.[28,30]

https://dx.doi.org/10.1021/acscatal.0c00794
ACS Catal. 2020, 10, 6546−6560

As evidenced by the energy partitioning and kinetic studies here, it is necessary to consider both thermodynamic and mechanistic implications for the applicability of PAC technologies, nominally the fourth major observation of this work. The decomposition of N_2O on metal oxide catalysts is often expressed using Langmuir−Hinshelwood (L-H) or Eley−Rideal (E-R) models, schematically represented in

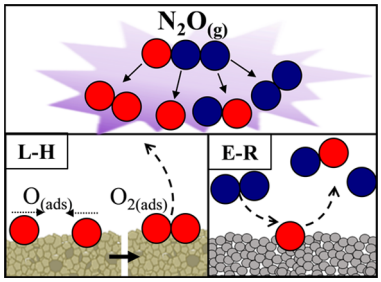

Figure 12. Schematic representation of plasma−catalyst interactions; example Langmuir−Hinshelwood (L-H) and Eley−Rideal (E-R) mechanisms are depicted.

Figure 12. Reactions 9 and 10 depict a possible N_2O decomposition pathway via an L-H mechanism

$$2N_2O_{(g)} + (*) \rightarrow 2N_{2(g)} + 2O^*_{(abs)} \quad (9)$$

$$2O^*_{(abs)} \rightarrow O_{2(g)} + (*) \quad (10)$$

where (*) symbolizes an active site on the catalyst surface. Within this mechanism scheme, the adsorbed surface oxygen migrates from one active site to another to form O_2 by recombination, ultimately the rate-determining step in the decomposition of N_2O, described above.[8] As shown in reactions 5 and 6, the PAC decomposition of N_2O produces atomic O and NO radicals, which can then potentially regenerate the active sites of the catalyst by recombining on the surface and desorbing. The O_{1s} binding environment for adsorbed oxygen is 532.1 eV, often documented in the evaluation of TiO_2 materials,[52] which overlaps with the Si−O−Al binding environment. Thus, increase in the Si−O−Al peak area in Figure 11e is likely the result of the plasma creating oxygen vacancies in the material, leading to a slight increase in the amount of Si at the surface. Although there are slight differences in the surface chemistry of zeolite materials after plasma processing, the material morphology remained largely unchanged (Figure S5).

Within the E-R mechanism, a chemisorbed molecule or atom interacts with a gas-phase species. The reaction of an $N_2O_{(g)}$ molecule interacting with $O_{(ads)}$ is depicted in reaction 11

$$O_{(ads)} + N_2O_{(g)} \rightarrow N_2 + O_{2(ads)} \rightarrow N_{2(g)} + O_{2(g)} \quad (11)$$

The E-R mechanism is considered rare in thermal catalysis because of the timescale of gas-phase surface interactions (picoseconds), reaction orientation, and entropy considerations.[53] Moreover, the E-R mechanism requires that a species from the gas phase interacts with adsorbed species; thus, the probability for such a collision can be low.[53] Using DFT calculations to study N_2O decomposition from a CaS(100) surface, Wu et al. calculated that the reaction of $N_2O_{(g)}$ and $O_{(ads)}$ to form $O_{2(ads)}$ (reaction 10) required 1.863 eV, whereas the removal of $O_{(ads)}$ from the surface by binding with neighboring $O_{(ads)}$ via the L-H mechanisms (reactions 9 and 10), depicted in Figure 12, required 1.877 eV.

Within a N_2O PAC system, $N_{2(g)}$ can react with $O_{(ads)}$, subsequently desorbing to form NO via an E-R pathway, depicted in Figure 12. These reaction products can undergo additional pathways (reaction 7) to form gas-phase species measured via optical spectroscopy. Zaharia et al. experimentally demonstrated an E-R reaction pathway when an O-covered Ru(0001) crystal was exposed to a molecular beam of nitrogen atoms and molecules. Within the initial stages of exposure, $O_{(ads)}$ interacts with $N_{2(g)}$ or $N_{(g)}$ from the beam, forming $NO_{(g)}$ species. The authors determined that as O coverage decreases and the adsorbed N coverage increased, the initial flux of NO is rapidly attenuated and a concomitant increase in $N_{2(g)}$ is documented.[54] The experimental determination of E-R pathways using molecular beams interacting with a material suggests that these reaction processes can occur within the PAC systems studied herein. Furthermore, modification of the direct E-R mechanisms proposes that an indirect, hot-atom pathway occurs when a gas-phase atom interacts and rebounds from the surface several times before colliding and reacting with an adsorbed species.[53] Regardless of the pathway, the removal of adsorbed oxygen to regenerate the active site of the catalyst is a critical step. Within a single-stage system, the zeolite catalysts benefited from direct plasma interactions, resulting in the smallest amount of NO in the discharge. A two-stage, pre-plasma configuration was deemed optimal for the Pt powder constructs, reducing the amount of NO compared to the native system without the detrimental oxidation effects caused by plasma exposure.

By obtaining a fundamental understanding of plasma−catalyst systems, efforts can focus on determining the most effective catalyst in conjunction with optimal design, configuration, and plasma operating conditions.[55] A plethora of variables can dominate these plasma−material interactions, including electron impact reactions and gas-phase neutral reactions, as well as a multitude of surface reactions. These interactions become progressively convoluted as the complexity of the systems increases. Suárez et al. studied the influence of a 2 vol % water vapor addition to an N_2O feed gas, which resulted in a decrease in catalytic activity with Rh-γ-Al_2O_3-sepiolite monolithic catalysts.[13] A similar effect was observed upon the addition of NH_3, suggesting that NH_X and OH species tend to adsorb at the same sites as N_2O, thereby reducing the number of active sites available for the decomposition of nitrous oxide and consequently yielding a decrease in catalytic activity.[13] Shown in Figure 3, as applied rf power increases to 175 W, [OH] increases when Pt nanopowder and microstructured zeolite materials are present. Thus, it is likely that OH is generated from plasma−catalyst interactions. To probe this further, Pt nanopowder and zeolite materials were oven-calcinated at 150 °C for 3 h to remove absorbed H_2O. Shown in Figure S3, the amount of OH in the discharge only slightly decreased at P = 175 W for the oven-calcinated zeolite data. This clearly indicates that $OH_{(g)}$ forms from oxygen species on the catalyst surface as opposed to being formed from gas-phase decomposition or recombination reactions of hydrogen or water contaminants in the system. Furthermore, with $OH_{(g)}$, we observe enhanced NO decomposition. Thus, reactions between N_2O and the catalysts appear to increase N_2O and NO conversion.

https://dx.doi.org/10.1021/acscatal.0c00794
ACS Catal. 2020, 10, 6546−6560

Ultimately, we believe there is still much work to be done to further understand the underlying mechanisms involved in the plasma−catalytic decomposition of N_2O. Nevertheless, the data presented herein clearly demonstrate that not only does the plasma alter the surface of catalytic materials, but the presence of both micro- and nanostructured catalytic materials clearly alters energy partitioning and reaction dynamics within the gas phase of the plasma.

5. SUMMARY

A comprehensive understanding of plasma-material interactions must necessarily include processes that occur at surfaces. Ultimately, many of our results demonstrate that the presence of a material in a plasma can dramatically alter the gas-phase chemistry of the system, from both a kinetics perspective and an energetics perspective. Although this might seem obvious, few studies have appropriately documented these effects. Within a N_2O rf ICP, N_2 emissions rise to an apparent steady state, whereas NO emissions approach a local maximum and a subsequent decay, where the addition of a catalyst had a minimal impact on measured rate constants. Steady-state energetics revealed that the addition of Pt and zeolite catalysts results in a pronounced decrease in the vibrational temperature of excited-state N_2. The vibrational temperature of NO species seems to depend more on chemical nature compared to morphology; both Pt catalysts had little to some quenching effects on T_V, where the addition of a zeolite pellet yielded an increase in T_V (NO). Moreover, this study epitomized the necessity to examine each portion of the PAC system (i.e., the plasma, the plasma−surface interface, and corresponding material analyses). Post plasma exposure material characterization revealed that the plasma effectively poisons the Pt materials through oxidation, resulting in poorer performance in the single-stage system, whereas the bulk and surface properties of the zeolites were nominally unaffected by the plasma. This line of scientific inquiry should be expanded to more complex mixed-gas systems, ultimately studying systems that resemble exhaust systems and atmospheric pollutants.

ASSOCIATED CONTENT

Supporting Information

The Supporting Information is available free of charge at https://pubs.acs.org/doi/10.1021/acscatal.0c00794.

Representative TR-OES and energy partitioning fits for N_2 and NO species within N_2O plasmas, OES actinometry and XPS data assessing oven-calcinated samples, as well as additional material characterization data (PDF)

AUTHOR INFORMATION

Corresponding Author

Ellen R. Fisher − *Department of Chemistry, Colorado State University, Fort Collins, Colorado 80523-1872, United States;* orcid.org/0000-0001-6828-8600; Email: Ellen.Fisher@ColoState.Edu

Author

Angela R. Hanna − *Department of Chemistry, Colorado State University, Fort Collins, Colorado 80523-1872, United States*

Complete contact information is available at: https://pubs.acs.org/10.1021/acscatal.0c00794

Notes

The authors declare no competing financial interest.

ACKNOWLEDGMENTS

This work was supported by the National Science Foundation (NSF CBET − 1803067) and the American Chemical Petroleum Research Fund (ACS PRF 59776 − ND6). The authors thank the staff of the CSU Central Instrument Facility for assistance with the XPS, XRD, and SEM analyses.

REFERENCES

(1) Ravishankara, A. R.; Daniel, J. S.; Portmann, R. W. Nitrous Oxide (N_2O): The Dominant Ozone-Depleting Substance Emitted in the 21st Century. *Science* **2009**, *326*, 123.

(2) *Understanding Global Warming Potentials*. https://www.epa.gov/ghgemissions/understanding-global-warming-potentials (accessed June 3 2019).

(3) Shimizu, A.; Tanaka, K.; Fujimori, M. Abatement Technologies for N_2O Emissions in the Adipic Acid Industry. *Chemosphere: Global Change Sci.* **2000**, *2*, 425−434.

(4) Centi, G.; Generali, P.; dall'Olio, L.; Perathoner, S.; Rak, Z. Removal of N_2O from Industrial Gaseous Streams by Selective Adsorption over Metal-Exchanged Zeolites. *Ind. Eng. Chem. Res.* **2000**, *39*, 131−137.

(5) Groen, J. C.; Pérez-Ramírez, J.; Zhu, W. Adsorption of Nitrous Oxide on Silicalite-1. *J. Chem. Eng. Data* **2002**, *47*, 587−589.

(6) Wójtowicz, M. A.; Miknis, F. P.; Grimes, R. W.; Smith, W. W.; Serio, M. A. Control of Nitric Oxide, Nitrous Oxide, and Ammonia Emissions Using Microwave Plasmas. *J. Hazard. Mater.* **2000**, *74*, 81−89.

(7) Zhao, G.-B.; Hu, X.; Plumb, O. A.; Radosz, M. Energy Consumption and Optimal Reactor Configuration for Nonthermal Plasma Conversion of N_2O in Nitrogen and N_2O in Argon. *Energy Fuels* **2004**, *18*, 1522−1530.

(8) Wagner, C. The Mechanism of the Decomposition of Nitrous Oxide on Zinc Oxide as Catalyst. *J. Chem. Phys.* **1950**, *18*, 69−71.

(9) Steacie, E. W. R.; McCubbin, J. W. The Decomposition of Nitrous Oxide on the Surface of Platinum. I. The Retarding Effect of Oxygen. *J. Chem. Phys.* **1934**, *2*, 585−589.

(10) Ohno, Y.; Kimura, K.; Bi, M.; Matsushima, T. The Translational Energy of Desorbing Products in NO and N_2O Decomposition on Pd (110). *J. Chem. Phys.* **1999**, *110*, 8221−8224.

(11) Zhang, F.; Wang, X.; Zhang, X.; Turxun, M.; Yu, H.; Zhao, J. The Catalytic Activity of NiO for N_2O Decomposition Doubly Promoted by Barium and Cerium. *Chem. Eng. J.* **2014**, *256*, 365−371.

(12) Jo, J.-O.; Trinh, Q. H.; Kim, S. H.; Mok, Y. S. Plasma-Catalytic Decomposition of Nitrous Oxide over γ-Alumina-Supported Metal Oxides. *Catal. Today* **2018**, *310*, 42−48.

(13) Suárez, S.; Saiz, C.; Yates, M.; Martin, J. A.; Avila, P.; Blanco, J. Rh/γ-Al_2O_3−Sepiolite Monolithic Catalysts for Decomposition of N_2O Traces. *Appl. Catal., B* **2005**, *55*, 57−64.

(14) Trinh, Q.-H.; Kim, S. H.; Mok, Y. S. Removal of Dilute Nitrous Oxide from Gas Streams Using a Cyclic Zeolite Adsorption−Plasma Decomposition Process. *Chem. Eng. J.* **2016**, *302*, 12−22.

(15) Zhang, B.; He, G.; Shan, Y.; He, H. Experimental and DFT Study of the Adsorption of N_2O on Transition Ion-Exchanged ZSM-5. *Catal. Today* **2019**, *327*, 177−181.

(16) Russo, N.; Mescia, D.; Fino, D.; Saracco, G.; Specchia, V. N_2O Decomposition over Perovskite Catalysts. *Ind. Eng. Chem. Res.* **2007**, *46*, 4226−4231.

(17) Adamovich, I.; Baalrud, S. D.; Bogaerts, A.; Bruggeman, P. J.; Cappelli, M.; Colombo, V.; Czarnetzki, U.; Ebert, U.; Eden, J. G.; Favia, P.; Graves, D. B.; Hamaguchi, S.; Hieftje, G.; Hori, M.; Kaganovich, I. D.; Kortshagen, U.; Kushner, M. J.; Mason, N. J.; Mazouffre, S.; Thagard, S. M.; Metelmann, H.-R.; Mizuno, A.; Moreau, E.; Murphy, A. B.; Niemira, B. A.; Oehrlein, G. S.; Petrovic, Z. L.; Pitchford, L. C.; Pu, Y.-K.; Rauf, S.; Sakai, O.; Samukawa, S.; Starikovskaia, S.; Tennyson, J.; Terashima, K.; Turner, M. M.; van de

Sanden, M. C. M.; Vardelle, A. The 2017 Plasma Roadmap: Low Temperature Plasma Science and Technology. *J. Phys. D: Appl. Phys.* **2017**, *50*, 323001.
(18) Fan, X.; Kang, S.; Li, J.; Zhu, T. Formation of Nitrogen Oxides (N_2O, NO, and NO_2) in Typical Plasma and Plasma-Catalytic Processes for Air Pollution Control. *Water, Air, Soil Pollut.* **2018**, *229*, 351.
(19) Whitehead, J. C. Plasma-Catalysis: The Known Knowns, the Known Unknowns, and the Unknown Unknowns. *J. Phys. D: Appl. Phys.* **2016**, *49*, 243001 (243024pp).
(20) Kim, H.-H.; Teramoto, Y.; Ogata, A.; Takagi, H.; Nanba, T. Plasma Catalysis for Environmental Treatment and Energy Applications. *Plasma Chem. Plasma Process.* **2016**, *36*, 45−72.
(21) Whitehead, J. C. Plasma Catalysis: A Solution for Environmental Problems. *Pure Appl. Chem.* **2010**, *82*, 1329.
(22) Affonso Nóbrega, P. H.; Rohani, V.; Fulcheri, L. Non-Thermal Plasma Treatment of Volatile Organic Compounds: A Predictive Model Based on Experimental Data Analysis. *Chem. Eng. J.* **2019**, *364*, 37−44.
(23) Barboun, P.; Mehta, P.; Herrera, F. A.; Go, D. B.; Schneider, W. F.; Hicks, J. C. Distinguishing Plasma Contributions to Catalyst Performance in Plasma-Assisted Ammonia Synthesis. *ACS Sustainable Chem. Eng.* **2019**, *7*, 8621−8630.
(24) Dębek, R.; Azzolina-Jury, F.; Travert, A.; Maugé, F. A Review on Plasma-Catalytic Methanation of Carbon Dioxide − Looking for an Efficient Catalyst. *Renewable Sustainable Energy Rev.* **2019**, *116*, 109427.
(25) Hur, M.; Lee, J. O.; Lee, J. Y.; Kang, W. S.; Song, Y.-H. Abatement Characteristics of N_2O in Low-Pressure Plasma Reactor. *Plasma Sources Sci. Technol.* **2015**, *25*, No. 015008.
(26) Fan, X.; Kang, S.; Li, J.; Zhu, T. Conversion of Dilute Nitrous Oxide (N_2O) in N_2 and N_2−O_2 Mixtures by Plasma and Plasma-Catalytic Processes. *RSC Adv.* **2018**, *8*, 26998−27007.
(27) Guillemot, M.; Castel, B. Workplace Nitrous Oxide Sampling: Alternative Adsorbents. *Ind. Eng. Chem. Res.* **2015**, *54*, 7760−7765.
(28) Hanna, A. R.; Blechle, J. M.; Fisher, E. R. Using Fundamental Spectroscopy to Elucidate Kinetic and Energetic Mechanisms within Environmentally Relevant Inductively Coupled Plasma Systems. *J. Phys. Chem. A* **2017**, *121*, 7627−7640.
(29) Zhang, Y.-R.; Van Laer, K.; Neyts, E. C.; Bogaerts, A. Can Plasma be Formed in Catalyst Pores? A Modeling Investigation. *Appl. Catal., B* **2016**, *185*, 56−67.
(30) Blechle, J. M.; Hanna, A. R.; Fisher, E. R. Determination of Internal Temperatures Within Nitric Oxide Inductively Coupled Plasmas. *Plasma Processes Polym.* **2017**, 1700041.
(31) Hanna, A. R.; Van Surksum, T. L.; Fisher, E. R. Investigating the Impact of Catalysts on N_2 Rotational and Vibrational Temperatures in Low Pressure Plasmas. *J. Phys. D: Appl. Phys.* **2019**, *52*, 345202.
(32) Cuddy, M. F.; Fisher, E. R. Contributions of CF and CF_2 Species to Fluorocarbon Film Composition and Properties for C_xF_y Plasma-Enhanced Chemical Vapor Deposition. *ACS Appl. Mater. Interfaces* **2012**, *4*, 1733−1741.
(33) Luque, J.; Crosley, D. R. *LIFBASE: Database and Spectral Simulation Program (Version 1.5)*; 1999.
(34) Laux, C. O. In *Radiation and Nonequilibrium Collisional-Radiative Models*; von Karman Institute Lecture Series, Physico-Chemical Modeling of High Enthalpy and Plasma Flows, Rhode-Saint-Gense, Belgium, Fletcher, D.; Charbonnier, J.-M.; Sarma, G. S. R.; Magin, T., Eds. Rhode-Saint-Gense: Belgium, 2002.
(35) Shah, M. A. Growth of Uniform Nanoparticles of Platinum By an Economical Approach at Relatively Low Temperature. *Sci. Iran.* **2012**, *19*, 964−966.
(36) Alexander, M. R.; Short, R. D.; Jones, F. R.; Michaeli, W.; Blomfield, C. J. A Study of HMDSO/O_2 Plasma Deposits Using a High-Sensitivity and -Energy Resolution XPS Instrument: Curve Fitting of the Si 2p Core Level. *Appl. Surf. Sci.* **1999**, *137*, 179−183.
(37) Biino, G. G.; Gröning, P. X-ray Photoelectron Spectroscopy (XPS) Used as a Structural and Chemical Surface Probe on Aluminosilicate Minerals. *Eur. J. Mineral.* **1998**, *10*, 423−438.
(38) Austin, J. M.; Smith, A. L. S. Decomposition of N_2O in a Glow Discharge. *J. Phys. D: Appl. Phys.* **1973**, *6*, 2236−2241.
(39) Neyts, E. C.; Ostrikov, K. K.; Sunkara, M. K.; Bogaerts, A. Plasma Catalysis: Synergistic Effects at the Nanoscale. *Chem. Rev* **2015**, *115*, 13408−13446.
(40) Zhang, Y.-R.; Neyts, E. C.; Bogaerts, A. Influence of the Material Dielectric Constant on Plasma Generation inside Catalyst Pores. *J. Phys. Chem. C* **2016**, *120*, 25923−25934.
(41) Chen, H.; Yue, J.; Li, Y.; Yi, C.; Yang, B.; Qi, S. Catalytic Activity Prediction of Different Metal Surfaces for N_2O Catalytic Decomposition by Density Functional Theory. *Comput. Theor. Chem.* **2015**, *1057*, 1−6.
(42) Wu, L.; Qin, W.; Hu, X.; Ju, S.; Dong, C.; Yang, Y. Decomposition and Reduction of N_2O on CaS (100) surface: A Theoretical Account. *Surf. Sci.* **2015**, *632*, 83−87.
(43) Konsolakis, M. Recent Advances on Nitrous Oxide (N_2O) Decomposition over Non-Noble-Metal Oxide Catalysts: Catalytic Performance, Mechanistic Considerations, and Surface Chemistry Aspects. *ACS Catal.* **2015**, *5*, 6397−6421.
(44) Mann, M. N.; Fisher, E. R. Perspectives on Antibacterial Performance of Silver Nanoparticle-Loaded Three-Dimensional Polymeric Constructs. *Biointerphases* **2018**, *13*, 06E404.
(45) Lee, D. H.; Kim, T. N2O Decomposition by Catalyst-Assisted Cold Plasma. In *20th International Symposium Plasma Chemistry*; Philadelphia, USA, 2012.
(46) Larsson, R. A Model of Selective Energy Transfer at the Active Site of the Catalyst. *J. Mol. Catal.* **1989**, *55*, 70−83.
(47) Larsson, R. Concluding Remarks on the Theory of Selective Energy Transfer and Exemplification on a Zeolite Kinetics Study. *Monatshefte für Chemie - Chemical Monthly* **2013**, *144*, 21−28.
(48) Larsson, R. Propane Dehydrogenation Catalyzed by ZSM-5 Zeolites. A Mechanistic Study Based on the Selective Energy Transfer (SET) Theory. *Molecules* **2015**, *20*, 2529−2535.
(49) Hanna, A. R.; Fisher, E. R. Investigating Recent Developments and Applications of Optical Plasma Spectroscopy: A Review. *J. Vac. Sci. Technol., A* **2020**, *38*, No. 020806.
(50) Larsson, R. Zeolite Catalysis and Molecular Vibrations. *Catal. Today* **1988**, *3*, 387−394.
(51) Larsson, R. Isokinetic Effects in Ethane Hydrogenolysis and Their Relation to the Mechanism of the Reaction. *Catal. Lett.* **1991**, *11*, 137−148.
(52) Cao, Y.; Meng, Q.; Yang, W.; Yao, J.; Shu, Y.; Wang, W.; Chen, G. Effect of Plasma Treatment on Surface Properties of TiO_2 Nanoparticulate Films. *Colloids Surf., A* **2005**, *262*, 181−186.
(53) Prins, R. Eley−Rideal, the Other Mechanism. *Top. Catal.* **2018**, *61*, 714−721.
(54) Zaharia, T.; Kleyn, A. W.; Gleeson, M. A. Eley-Rideal Reactions with N Atoms at Ru(0001): Formation of NO and N_2. *Phys. Rev. Lett.* **2014**, *113*, No. 053201.
(55) Whitehead, J. C. Plasma-Catalysis: Is it just a question of scale? *Front. Chem. Sci. Eng.* **2019**, *13*, 264−273.

https://dx.doi.org/10.1021/acscatal.0c00794
ACS Catal. 2020, 10, 6546−6560